A Bio-inspired Dendritic MoO_x Electrocatalyst for Efficient Electrochemical Nitrate Reduction to Ammonia

*Yuan-Zi Xu, Daniel F. Abbott, Robin N. Dürr, Tran Ngoc Huan, Victor Mougel**

Yuan-Zi Xu, Daniel F. Abbott, Robin N. Dürr, Victor Mougel
Department of Chemistry and Applied Biosciences, ETH Zürich, Zürich, Switzerland
E-mail: mougel@inorg.chem.ethz.ch

Tran Ngoc Huan
Laboratoire de Chimie des Processus Biologiques, UMR CNRS 8229, Collège de France, Université Pierre et Marie Curie, 11 Place Marcelin Berthelot, 75005 Paris, France

Keywords: Bio-inspired, Reduced molybdenum oxide, Oxygen vacancies, Electrocatalyst, Nitrate Reduction

Abstract: Drawing inspiration from the nitrate reductase enzymes, which catalyze nitrate to nitrite in nature, here we introduce a bio-inspired, reduced molybdenum oxide (MoO_x) shell that is grown on top of a dendritic nickel foam core (Ni_{NF}). The resulting MoO_x/Ni_{NF} material is prepared via a facile, two-step electrodeposition strategy using commercially available, low-cost precursors. This catalytic material displays a remarkable faradaic efficiency (FE) of 99% at −0.5 V vs. RHE and a high ammonia (NH_3) yield rate of up to 4.29 mmol h^{-1} cm^{-2} at −1.0 V vs. RHE in neutral media. Most importantly, MoO_x/Ni_{NF} exhibits exceptional stability for the nitrate reduction reaction (NO_3RR), maintaining operation for over 3,100 hours at a high current density of −650 mA cm^{-2}, with a yield rate of 2.6 mmol h^{-1} cm^{-2} and a stable average NH_3 FE of ~83%. We show, through combined XPS and *in-situ* Raman spectroscopy, that the pronounced affinity of MoO_x/Ni_{NF} for nitrate is associated with a substantial presence of oxygen vacancies within the material.

Introduction

The excessive use of nitrogen-based fertilizers for agriculture over the last century has resulted in

a global net increase of the amount of reactive nitrogen species in the environment.[1] Nitrates represent the most problematic byproduct from over fertilization, as its high solubility and environmental mobility endangers natural ecosystems via eutrophication, while also presenting a great risk to human health due to the consumption of nitrate-polluted water sources.[2] Electrocatalytic approaches have been previously proposed as a promising strategy for water denitrification, but initial studies targeted the reduction of nitrate to dinitrogen, owing to its ease of separation from the polluted water sources.[3] However, this reaction involves the formation of a N≡N triple bond from two nitrate molecules, which represents a significant challenge as many reaction byproducts and intermediates, such as nitrite, nitrous oxide, hydroxylamine or ammonia, can be released along the reaction path and lower the reaction selectivity to N_2.[3b, 4]

Driven by the current surge of electrochemical approaches for the preparation of key commodity chemicals, the selective nitrate reduction reaction (from here on referred to as NO_3RR) to ammonia was recently envisioned, as it provides an alternative route to produce ammonia from waste sources while significantly lowering the selectivity challenge previously associated to denitrification. It remains a kinetically challenging eight electron / nine proton reduction process and selectivity issues towards the competitive hydrogen evolution reaction (HER) must be addressed.[5]

Despite being only recently a focus of study, impressive selectivity to ammonia and high ammonia partial current densities have been reported under neutral conditions (**Table S1**).[6] However, among the remaining challenges for the electrocatalytic reduction of nitrate to ammonia, the identification of earth-abundant metal-based catalysts displaying high stability while maintaining high selectivity and high partial current densities at neutral pH would constitute a key step for the development of water denitrification processes.

In nature, the first key enzymes catalyzing the reduction of nitrate anions are nitrate reductase enzymes (NRases), which catalyze the two-electron reduction of nitrate to nitrite in neutral media.[7] A central step in the nitrate reduction by respiratory NRases is the coordination of the weakly coordinating nitrate anions to a low-valent Mo(IV) center, followed by its reduction to a nitrite anion via an oxygen atom transfer to the Mo site, yielding a Mo(VI) oxo species. The active site of the NRases is regenerated via two consecutive proton-coupled electron transfer (PCET) steps on this parent Mo(VI) oxo species.[7a, 8]

Taking the molybdenum nitrate reductase enzymes as inspiration, oxo-containing molybdenum

sulfide materials have been recently reported to catalyze the NO_3RR with high selectivity and stability.[9] In addition, we recently reported Fe-substituted two-dimensional molybdenum carbide MXenes as highly active catalysts for the NO_3RR with a faradaic efficiency (FE) for ammonia of 70% and a yield rate of 12.9 μmol h^{-1} mg^{-1}.[10] We identified that promoting the formation of surface O vacancies and the corresponding generation of coordinatively unsaturated low-valent Mo oxo was the essential step to enable catalytic activity, in close analogy to the proposed mechanism of Mo-based NRase enzymes. However, both of these catalysts displayed modest ammonia partial current densities overall, mainly hampered by their high activity for HER. This was particularly evident in the case of molybdenum sulfide-based materials, where the intense evolution of H_2 resulted in reduced selectivity when operated at high current densities.

In the present study, we report on the development of a low-valent Mo-oxide (MoO_x) catalyst for NO_3RR, capitalizing on the strong binding energy of oxygen species on reduced Mo oxide materials. Owing to the presence of oxygen vacancies,[11] the bio-inspired activation of nitrate anions at the Mo centers are promoted while the competing HER is minimized. Indeed, compared to the Mo sulfide and carbide materials used in the above-mentioned studies, undoped Mo oxides are known to exhibit only modest HER activity in neutral media.[12] Electrochemical deposition under limiting current conditions is known to produce dendritic metallic materials of high porosity, mainly resulting from the concomitant generation of hydrogen bubbles. The so-called dynamic hydrogen bubble templating (DHBT) approach, as developed in our group[13] and others,[14] has proven to be a successful strategy for electrocatalysts design, providing high surface area materials with improved mass transport and potential confinement effects.[15] Leveraging on this synthetic approach, we introduce here a high surface area MoO_x material generated by electrodeposition that displays unprecedented NH_3 selectivity, low overpotential, and high NH_3 partial current densities during NO_3RR in neutral media.

The electrodeposition of metallic molybdenum, required to generate high surface area materials via a DHBT approach, is however very challenging,[16] and constitute the main hurdle for the development of such materials. In this work, we circumvented that fact by utilizing high surface area dendritic Ni structures generated upon electrodeposition at high current densities on a Ni foam (Ni_{NF}) as a support for electrodeposited MoO_x. Besides being one of the most commonly used high surface area metal electrode materials, nickel appear here as a support of choice given

the fact that it had been reported to enhance adhesion of electrodeposited Mo black materials.[17] We demonstrate here that the electrodeposition of ammonium molybdate on a dendritic Ni material at high current densities yields a high surface area reduced Mo oxide catalyst, MoO_x/Ni_{NF}. MoO_x/Ni_{NF} exhibits unique catalytic performances for NO_3RR, with a high faradaic efficiency of 99% at −0.5 V vs. RHE and an NH_3 production rate of 4.29 mmol h^{-1} cm^{-2} at −1.0 V vs. RHE. This exceptional catalytic activity and selectivity in neutral media allowed us to investigate long-term operation under industrially relevant conditions. MoO_x/Ni_{NF} displayed a remarkable stability when operated continuously for over 4 months at −650 mA cm^{-2}.

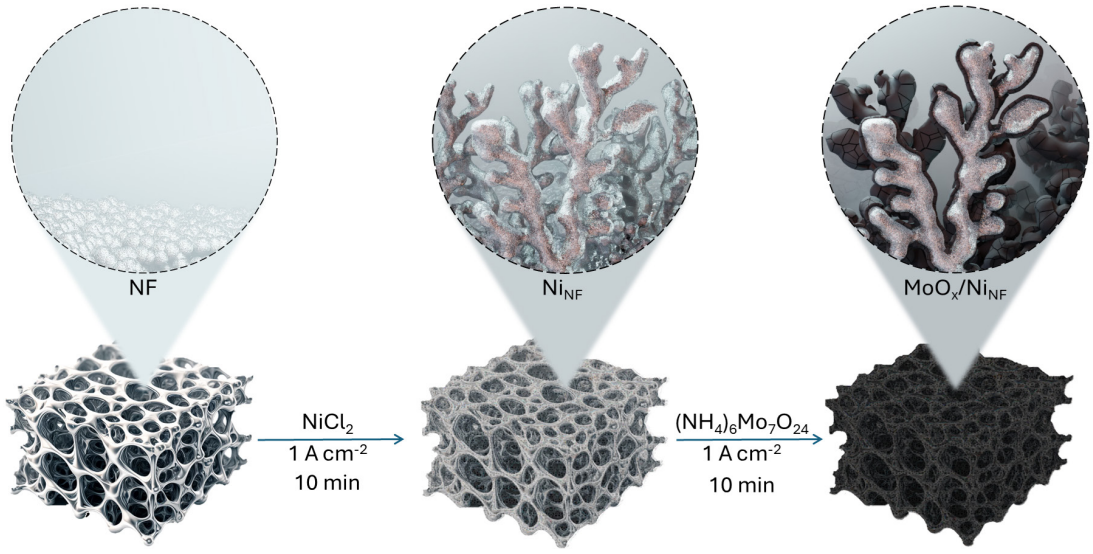

Figure 1. Schematic representation of the electrochemical synthesis of MoO_x/Ni_{NF}.

Results and Discussion

The fabrication of the high surface area MoO_x/Ni_{NF} material is carried out in two steps, as is schematically illustrated in **Figure 1**. The first step consists of generating a high surface area Ni support via the electrodeposition of Ni from an aqueous $NiCl_2$ solution above the limiting current density (i.e. at −1 A cm^{-2}) on a commercial nickel foam (NF) substrate (See **Figure S1** for SEM characterization of the bare NF). This process results in a porous, mossy Ni dendrite-like structure with large cavities, as observed in the scanning electron microscopy (SEM) images (**Figure 2a-c**). This high surface area material, now referred to as Ni_{NF}, was subsequently used as a support for MoO_x. A black, Mo-based deposit (**Figure S2**) was obtained upon reductive electrodeposition of a dilute aqueous $(NH_4)_6Mo_7O_{24}$ solution in the presence of high acetate

concentrations at a high current density.[16a, b] The SEM images of MoO_x/Ni_{NF} presented in **Figure 2d-f** reveal that the overall structure of the Ni_{NF} support is maintained after the electrodeposition of MoO_x. The side view of MoO_x/Ni_{NF} further shows that the MoO_x is deposited as a layer that completely covers the dendrite-like Ni structures (**Figure 2f**). Cracks can be identified at the surface of the MoO_x layer, which may be due to the large residual tensile stress during deposition at high current density.[18] Furthermore, elemental mapping via energy-dispersive X-ray spectroscopy (EDX) shown in **Figure 2g-j** and **Figure S3** confirm the presence of Mo along with O on top of the Ni dendrites.

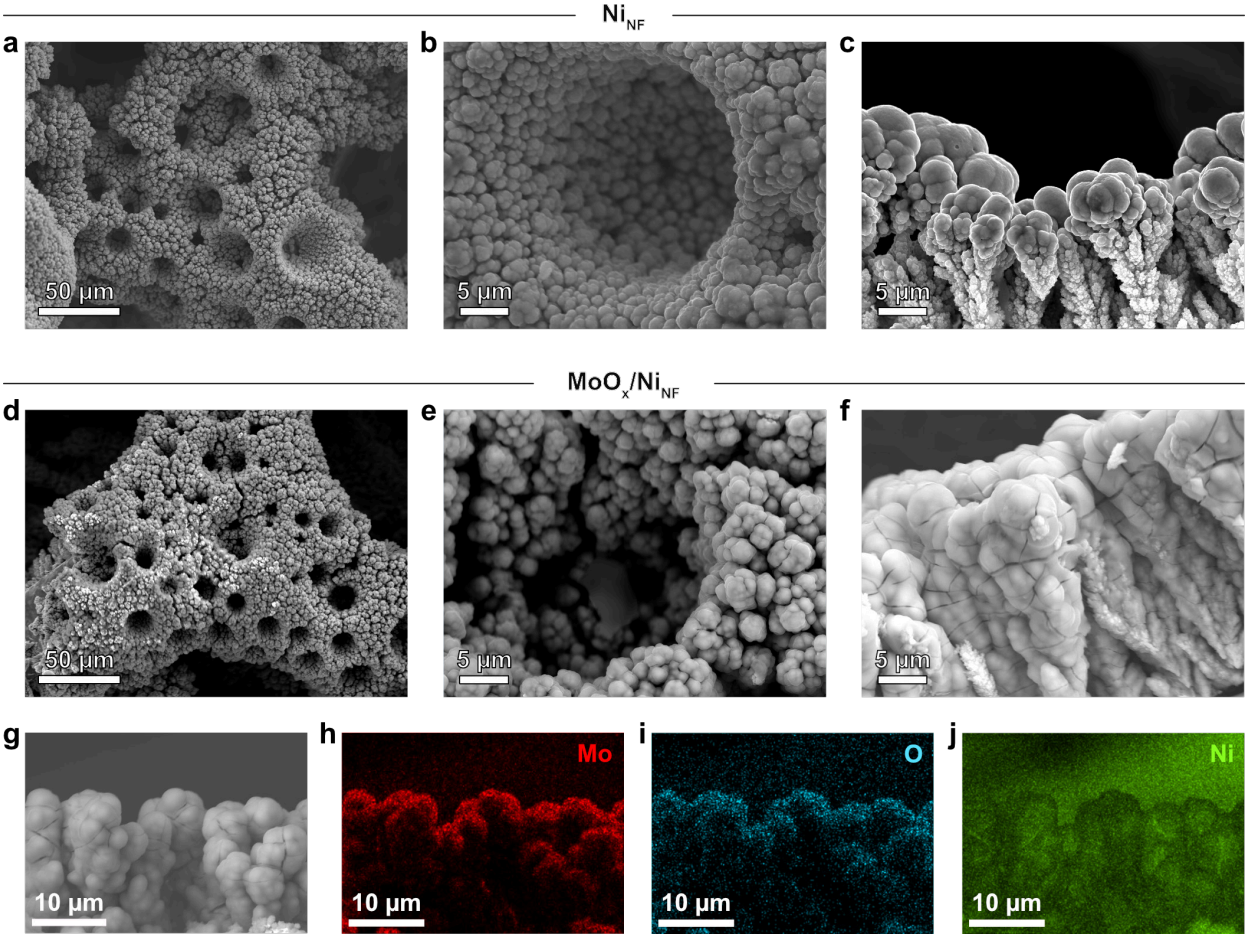

Figure 2. Secondary electron (SE) images of (**a-c**) Ni_{NF} and (**d-f**) MoO_x/Ni_{NF} with different resolutions. (**g**) SE image of the area of MoO_x/Ni_{NF} used for elemental mapping. (**h-i**) Elemental mapping of the area in (**g**) for Mo, O, and Ni.

To gain further insight into the structure and composition of the deposited layer, focused ion beam (FIB) cross sections of the electrode were prepared (**Figure 3a** and **Figure S4**). The SEM image of the FIB cross-section and the corresponding EDX maps shown in **Figure 3b-e** reveal the presence of a Ni core and a MoO_x shell of ca. 2 µm thickness, as is suggested by the co-

location of Mo and O. The cracks observed in the SEM images (**Figure 2f**) can be also observed in the cross-section image (**Figure 3a**). Scanning transmission electron microscopy (STEM) was then used to investigate the interface between the Ni core and MoO_x shell and the individual layers at higher resolution. The high-angle annular dark-field (HAADF) image of the MoO_x/Ni_{NF} interface is displayed in **Figure 3f** with golden circles highlighting the areas that were analyzed with selected area electron diffraction (SAED). The MoO_x layer displays only an amorphous halo with the absence of clear diffraction rings (**Figure 3g**) suggesting its amorphous nature, which is further supported by the absence of crystalline fringes in the high-resolution TEM image of the MoOx layer (**Figure S5a**, **b**). The Ni core was identified by lattice fringes with an interplanar spacing of 0.175 nm, which can be assigned to the (200) plane of metallic Ni (**Figure S5c**, **d**). The corresponding SAED pattern of the Ni core revealed several diffraction rings, assigned to the (111), (200), (220), (311), (222), (331), and (420) planes of metallic Ni (**Figure 3h**).

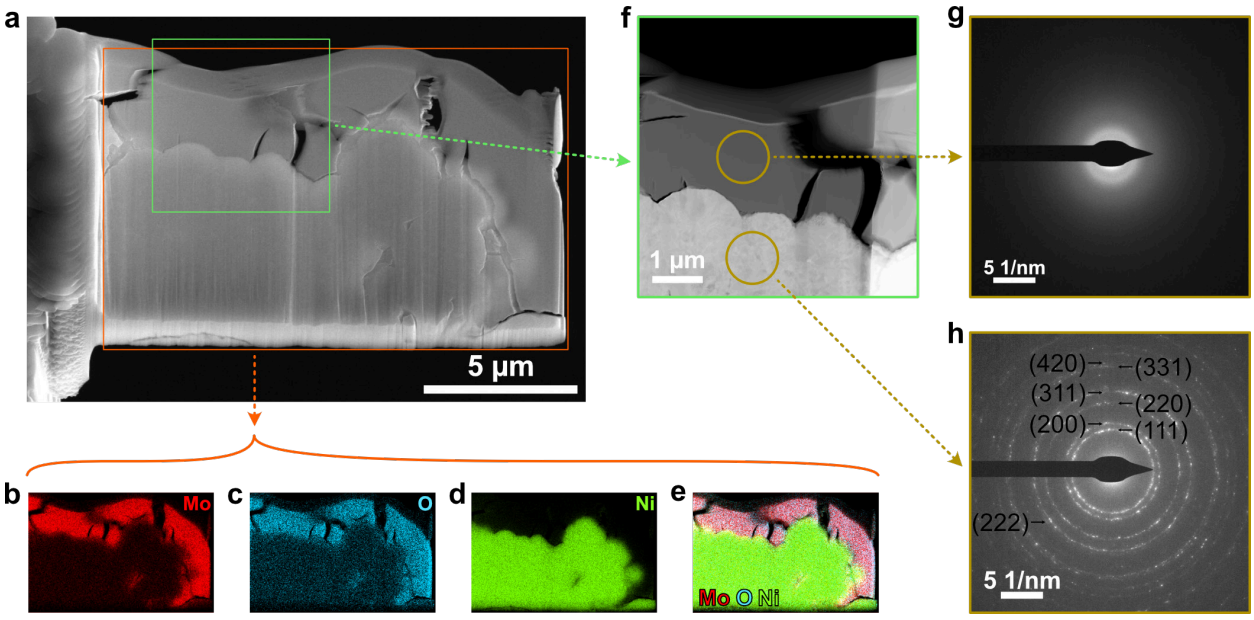

Figure 3. (**a**) SEM image of the FIB cut cross section with the orange and green rectangle showing the area of the elemental mapping (**b-e**) and HAADF imaging (**f**). (**b-d**) Mo, O, Ni EDX elemental mapping and (**e**) the overlay of those elements. (**f**) HAADF image with the golden circles indicating the regions used for SAED in (**g**) and (**h**) of the MoO_x and Ni layer, respectively.

The X-ray diffraction (XRD) pattern of the as-prepared sample is shown in **Figure S6** and reveals the characteristic peaks corresponding to the (111), (200), (220), (311), and (222) planes of cubic Ni at 44.51°, 51.85°, 76.37°, 92.94°, and 98.45°, respectively. No characteristic diffraction peaks of Mo oxide compounds were observed, corroborating the amorphous nature of

the layer as proposed by TEM analysis.

Despite the absence of crystalline Mo phases identified in the XRD pattern, however, the presence of MoO_x, as suggested by the EDX mapping, can be corroborated by the Raman spectrum of the material (**Figure S7**), which shows faint bands centered at 283 cm^{-1}, 377 cm^{-1} and 474 cm^{-1}. The broad nature of these bands, which are tentatively assigned to the wagging and the asymmetric stretching/bending mode of O-Mo-O in MoO_2,[19] is a good further indication of the amorphous nature of the molybdenum oxide layer

Lastly, X-ray photoelectron spectroscopy (XPS) depth profiling studies of MoO_x/Ni_{NF} were used to confirm the overall core-shell structure outlined above. The survey spectra collected as a function of etching time (**Figure S8a**) show that the Mo and Ni contents increase gradually from 13.4 to 17.8% and from 4.0 to 8.3%, respectively, as the etching time increases (**Table S2**). Simultaneously, it can be observed that the concentration of O gradually decreases (**Figure S8b** and **Table S2**). While the signal intensities corresponding to both the Ni 2p and Mo 3d peaks are present in all of the collected survey spectra, the Ni 2p peaks are weak in comparison to the Mo 3d and clearly become more pronounced as the surface is etched away, highlighting that the surface of the material is predominantly coated by Mo-based species. The high-resolution Mo 3d spectra recorded as a function of etching time reveal a significant development of the Mo surface layer with depth (**Figure 4a**). Particularly notable is the appearance of a shoulder at ca. 229 eV after only the first etching step (15 s), corresponding to the presence of metallic Mo, which continues to increase upon additional etching (**Figure S9**). Fitting of the Mo 3d peaks (**Figure 4b** and **Table S3**) before depth profiling reveals that the surface is predominantly constituted by Mo^{4+} (Mo $3d_{5/2}$ and $3d_{3/2}$ peaks at 230.7 and 233.8 eV) and Mo^{5+} species (Mo $3d_{5/2}$ and $3d_{3/2}$ peaks at 232.0 and 235.2 eV). After depth profiling, Mo^{4+} is still identified as the dominant species, co-existing with both Mo^{5+} and metallic Mo^0 species (Mo $3d_{5/2}$ and $3d_{3/2}$ peaks at ca. 228.7 and 231.9 eV). Overall, the depth profiling indicates the existence of a mixed-valent molybdenum oxide surface layer, which in turn suggests the presence of oxygen vacancies.[11] This notion is corroborated by the O 1s spectra (**Figure 4c**), which can be fitted into three separate peaks. The first peak at ca. 530.6 eV corresponds to lattice-bound oxygen (O_L), while the second peak at ca. 531.9 eV can be attributed to non-lattice oxygen, resulting from the formation of oxygen vacancies in the metal oxide layer and here assigned to as O_V in the XPS discussion, as has been reported previously.[11] The final peak at ca. 533.4 eV is attributed to

OH^- bonds. Depth profiling reveals that the contributions from each component do not change significantly with etching time, with the O_L and O_V always constituting roughly 65-70% and 25-29% of the signal, respectively, and O_{OH-} comprising only 4-7% (**Figure S10**, **Figure S11**, **Table S4**), indicating that the oxygen vacancy content is rather homogeneous throughout the mixed oxide layer. Ultimately, the above findings show that the as-prepared MoO_x/Ni_{NF} possesses a core-shell structure, wherein a Ni core is enveloped by an amorphous mixture of metallic Mo^0 and Mo oxides in the shell. Considering the high competition from HER in acid media and the instability of MoO_x in alkaline media, the catalytic activity of MoO_x/Ni_{NF} was evaluated in neutral media (0.1 M Na_2SO_4; pH = 6.8) containing 0.1 M NO_3^- in an H-cell setup (**Figure 5a-b**). Linear sweep voltammetry (LSV) experiments in the absence and presence of NO_3^- (**Figure 5a)** indicate that a significant enhancement in catalytic current is observed in neutral media in the presence of NO_3^-, suggesting the occurrence of NO_3RR. Comparison of the LSVs in **Figure 5a** shows that the onset potential for NO_3RR in 0.1 M Na_2SO_4 occurs at ca. −0.2 V (all reported potentials refer to the RHE scale) and that significant competition from the HER does not begin until <−0.7 V. To relate this current enhancement to NO_3RR catalytic activity, a series of 0.5 h chronoamperometric holds (CA) were carried out over the potential range of −0.6 V to −0.2 V.

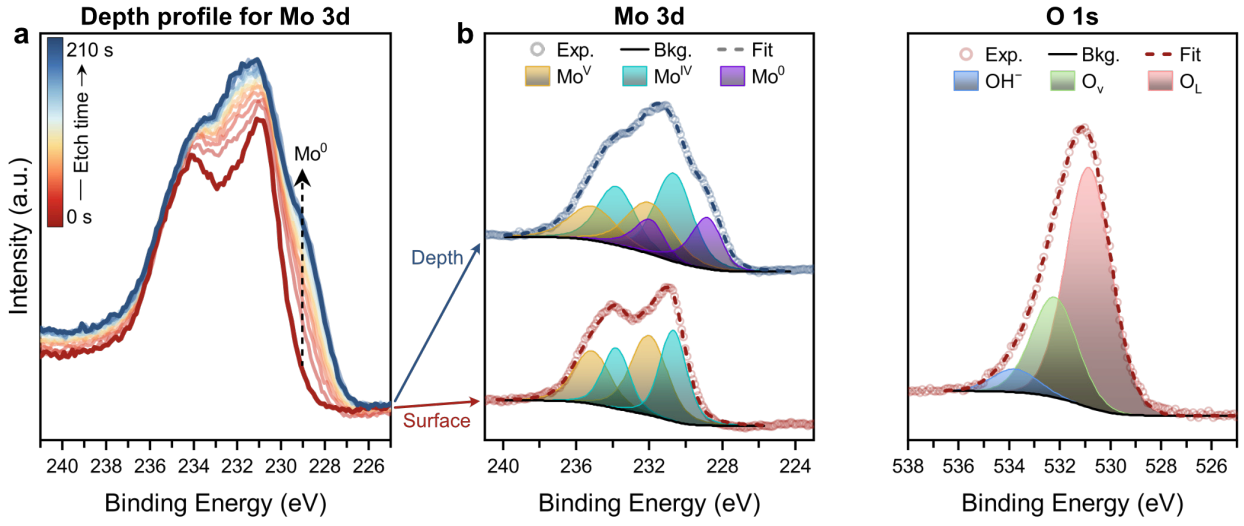

Figure 4. (**a**) XPS depth profiling study showing the development of Mo 3d orbital at 15 s etching intervals for up to 210 s. (**b**) Fitting of the Mo 3d region before etching (Surface, t = 0 s, bottom plot) and after etching (Depth, t = 210 s, top plot) with peaks assigned to oxidized Mo^V and Mo^{IV} and metallic Mo^0 species. (**c**) Fitting of the O 1s region at t = 0 s of the surface spectrum with peaks assigned to hydroxo (OH^-), oxygen vacancies (O_v), and lattice oxygen (O_L) species.

The reaction products, including NH_3, H_2, and NO_2^-, were quantified utilizing ^{1}H-NMR, gas chromatography (GC), and ion chromatography (IC), respectively (please refer to the SI and **Figures S12-15** for further details). The CA holds over this potential region and quantification of the generated NH_3 show an increase of the NH_3 faradaic efficiency (FE) from 63% to 80% as the potential is decreased from −0.2 to −0.5 V (**Figure 5b**). It can be observed that the maximum FE for NH_3 occurs after the FE for NO_2^- has decreased and before the FE for H_2 begins to increase at more cathodic potentials, signaling a potential-dependent competition between these three reactions for the same active site. In contrast, the NH_3 yield rate displays no peak and is shown to increase monotonically from 0.01 to 0.19 mmol h^{-1} cm^{-2} as the potential is decreased from −0.2 to −0.6 V (**Figure 5b**). However, the constrains on the performance of MoO_x/Ni_{NF} caused by the competing side reaction, in particular in a non-buffered media, indicate the necessity for further optimization of the reaction conditions. Notably, recent evidence suggests that adjusting the concentration of the supporting electrolyte could positively impact the selectivity of the NO_3RR.[6k] This effect is clearly demonstrated in **Figure S16a**, where we observe a substantial increase of the current densities achieved in the LSVs collected for MoO_x/Ni_{NF} in 1 M Na_2SO_4 with and without 0.1 M NO_3^- as compared to 0.1 M Na_2SO_4 (*cf.* **Figure 5a**). Current densities of −86, −129, and −143 mA cm^{-2} are reached at −0.4, −0.5 and −0.6 V in 1 M Na_2SO_4 containing 0.1 M NO_3^- as compared to just −20, −36, and −54 mA cm^{-2} in 0.1 M Na_2SO_4 containing 0.1 M NO_3^-. More importantly, the FE for NH_3 is shown to increase significantly, getting close to unity with an FE of 98% being observed at −0.5 V (**Figure S16b**). Accordingly, the yield rate and partial current density for NH_3 increases gradually from −0.2 to −0.6 V (**Figure S16c**). A large partial current density for ammonia, j_{NH3}, of ca. 157 mA cm^{-2} is achieved at −0.6 V, corresponding to an high yield rate of 0.73 mmol h^{-1} cm^{-2}, as compared to just ca. 42 mA cm^{-2} and 0.19 mmol h^{-1} cm^{-2} in the case of 0.1 M Na_2SO_4 with NO_3^-. Similar performances and FE were observed in the presence of ^{15}N-labeled NO_3^- (**Figure S17**), confirming that the generated NH_3 originates solely from the added NO_3^- and not from adventitious nitrogen sources. In the above cases, it should be noted that the electrolyte remained in a moderate pH range due to the large volume of electrolyte used despite raising the Na_2SO_4 concentration from 0.1 M to 1 M.

To investigate the potential contribution of the Ni support in the catalytic performances, the catalytic NO_3RR performances of the MoO_x/Ni_{NF} electrodes were compared with that of the

dendritic Ni_{NF} at a potential of −0.5 V. As shown in **Figure S18**, a high NH_3 yield rate and FE for NH_3 (0.53 mmol h^{-1} cm^{-2} and 83%, respectively) were observed for NO_3RR using Ni_{NF}. While high, the Ni_{NF} support performances remains lower than those of MoO_x/Ni_{NF} (NH_3 yield rate = 0.78 mmol h^{-1} cm^{-2}, FE_{NH3} = 98%). We observed that the lower selectivity of Ni_{NF} for ammonia production results from the competitive HER reaction, with H_2 being observed as the main secondary product on Ni_{NF}. This selectivity difference is not unexpected: the strong *H binding on Ni surfaces leads to favoring the HER over NO_3RR, except at very low overpotentials where Ni can have *H underpotential deposition that would not lead to HER.[20] To further assess this claim, we turned to electrochemical impedance spectroscopy (EIS) and cyclic voltammetry studies. The Nyquist plots of MoO_x/Ni_{NF} and Ni_{NF} are compared in **Figure S19**, where the resistance between the reference electrode and the working electrode (R_s) is assigned to the high frequency intercept of the impedance data with the Z' axis, and the charge transfer resistance (R_{ct}) was approximated from the intercepts of the circular fit of the impedance data with the Z' axis. First, the very small R_s values observed for both materials (R_s = 0.19 Ω and 0.56 Ω for MoO_x/Ni_{NF} and Ni_{NF}, respectively) highlights the importance of the direct deposit of the MoO_x catalyst on the high surface area conducting support constituted by Ni_{NF}, thereby minimizing any ohmic losses. Second, the circular fit estimates a smaller R_{ct} for MoO_x/Ni_{NF} (1.85 Ω) versus Ni_{NF} (3.73 Ω), indicating a faster electron transfer process under NO_3RR conditions for MoO_x/Ni_{NF} at −0.5 V, which agrees well with the overall higher catalytic current densities observed for MoO_x/Ni_{NF} compared to Ni_{NF}. In addition, we investigated the electrochemical surface area (ECSA) of the materials via the determination of their double-layer capacitances (C_{dl}) by cyclic voltammetry (**Figure S20**). It clearly demonstrates that the C_{dl} of Ni_{NF} (4.43 mF cm^{-2}) is significantly higher than that of the unmodified NF (0.35 mF cm^{-2}), showing an approximately 12.7-fold increase and suggesting that the electrodeposited Ni dendrite constructs a high surface area. Furthermore, the C_{dl} of MoO_x/Ni_{NF} (5.08 mF cm^{-2}) was slightly higher than that of Ni_{NF}, which we attribute to the cracks observed in the MoO_x layer.

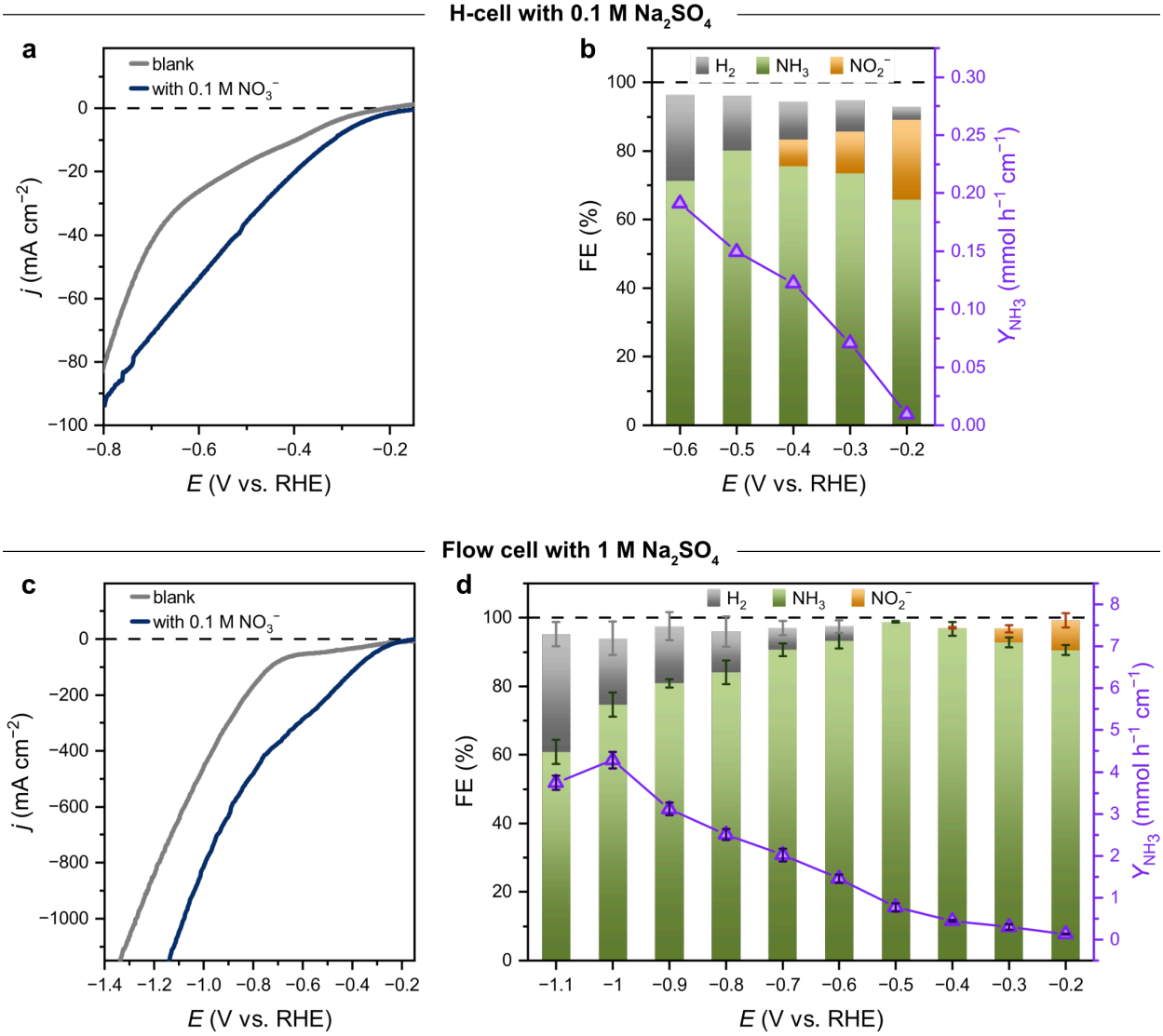

Figure 5. Electrochemical performance of MoO_x/Ni_{NF} in an H-cell containing 0.1 M Na_2SO_4 (top). (**a**) LSV in the absence (gray line) and presence of NO_3^- (dark blue line). (**b**) Applied potential-dependent FE for different reaction products with the corresponding NH_3 yield rates at the potentials applied (purple scatters). Electrochemical performance of MoO_x/Ni_{NF} in a flow cell with 1 M Na_2SO_4 (bottom). (**c**) LSV in the absence (gray line) and presence of NO_3^- (dark blue line). (**d**) FE at different applied potentials for different reaction products (bar diagram) and the obtained NH_3 yield at the corresponding potentials (purple scatters).

To gain insight in reaction intermediates formed during the electrochemical nitrate reduction process, *in situ* Raman spectroscopy studies were conducted. In **Figure 6a**, the Raman spectrum of MoO_x/Ni_{NF} during NO_3RR at different potentials is presented. Under open circuit potential (OCP) conditions, peaks observed in the spectra are assigned to SO_4^{2-} at 982 cm^{-1} and to free NO_3^- ions at ~1048 cm^{-1}.[21] Upon application of cathodic potentials, vibrational peaks at 731 and 1382 cm^{-1} gradually appear and are attributed to the N−O bending mode and ν_a modes of surface bound NO_3^-, respectively.[22] In contrast, the intensity of the same vibrational peaks increase more slowly for Ni_{NF} under the same conditions (**Figure 6b**),

suggesting a stronger adsorption of NO_3^- on MoO_x/Ni_{NF} than on Ni_{NF}, presumably favored by the oxygen vacancies in the MoO_x surface. Moreover, a vibrational peak at 1218 cm^{-1} emerges from −0.2 V and increases at more cathodic potentials for MoO_x/Ni_{NF}, which can be attributed to adsorbed NO_2 (*NO_2, nitrito orientation).[23] The presence of these intermediate species suggests the conversion of NO_3^- to *NO_2. Conversely, Raman peaks for absorbed *NO_2 on Ni_{NF} were not observed with decreasing potential from −0.2 to −0.6 V, corroborating the lower catalytic activity observed for Ni_{NF}. Last, the intermediate *ONO*$^-$ chelating mode (1298 cm^{-1}) is also observed on MoO_x/Ni_{NF} from −0.2 to −0.6 V, suggesting that NO_3RR proceeds via an alternative formation mode of nitrite association to the electrode surface.[23-24] The observation of these reaction intermediates is in good agreement with the proposed reaction mechanism for the reduction of nitrate to ammonia via the intermediacy of nitrite.

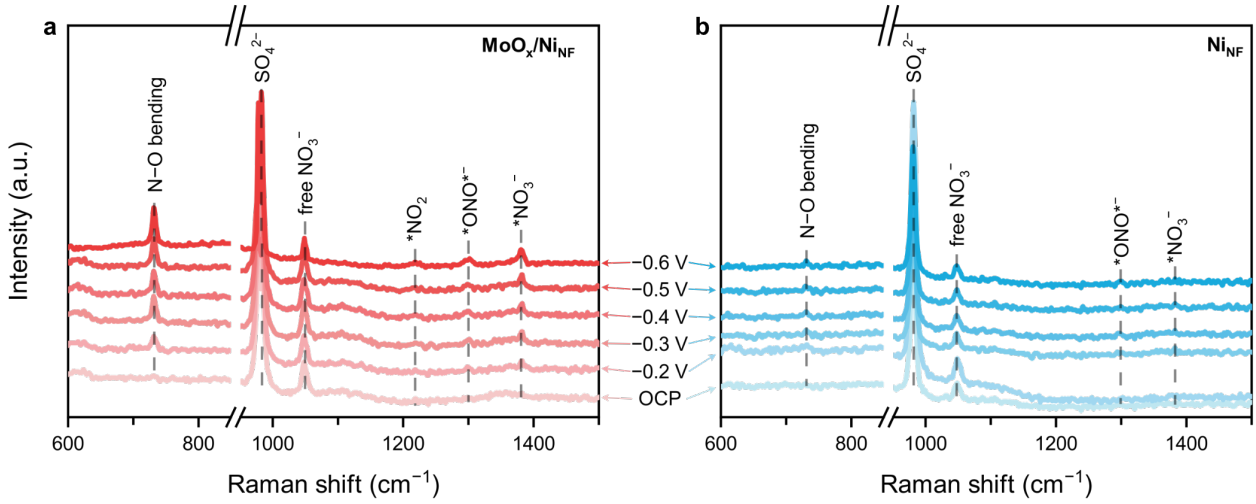

Figure 6. *In situ* Raman studies at different applied potentials for (**a**) MoO_x/Ni_{NF} and (**b**) Ni_{NF}.

Besides product selectivity, the stability is the other key criteria to consider when evaluating the industrial application potential of a catalyst. To assess the capability of MoO_x/Ni_{NF} to retain its functionality upon multiple cycles of an applied potential, a consecutive recycling test using the same piece of catalyst was carried out. MoO_x/Ni_{NF} retained very high performances in terms of NH_3 selectivity and yield rate over 12 consecutive recycling cycles at a constant potential of −0.5 V for 30 minutes each (**Figure S21**). However, we observed that the pH of the electrolyte in the cathodic compartment of the H-cell setup drifted from 7 to 14 within just 30 minutes of electrolysis, potentially limiting the long-term stability of the catalyst. In addition, the LSV in this condition reveals that at potentials below −0.6 V, the system operates in a regime where the mass transport of NO_3^- is limited by its concentration,

hampering the j_{NH3} and yield rate for NH_3 (**Figure S16a**). To circumvent both pH drift and NO_3^- mass transport limitation issues, and evaluate the application potential of MoO_x/Ni_{NF}, we investigated its catalytic performance in a flow cell to allow for the continuous delivery of fresh electrolyte to the cathode compartment. The LSV curves of MoO_x/Ni_{NF} operated in the flow conditions indicate a significant enhancement in current density, reaching over 1 A cm^{-2} at −1.1 V in the presence of 0.1 M NO_3^- (**Figure 5c**). Under these conditions, high ammonia FEs of over 90% are retained across a broad potential range from −0.2 to −0.7 V, while the competitive HER is essentially suppressed (below 10%, **Figure 5d**). At −1.0 V the MoO_x/Ni_{NF} catalyst demonstrates an NH_3 yield rate of up to 4.29 mmol h^{-1} cm^{-2} corresponding to a j_{NH3} value of 918.88 mA cm^{-2} (**Figure 5d**, **Figure S22**), surpassing previously reported NH_3-selective electrocatalysts (see **Table S1**). We further investigated the stability of MoO_x/Ni_{NF} at an applied current density of −125 mA cm^{-2}, corresponding to the potential at which the catalyst exhibits its highest FE of 98.8% for NH_3 production (i.e. −0.5 V), at which a stable working potential was observed for over 110 hours with negligible changes in the FE and a constant NH_3 production (**Figure S23)**. Post-electrolysis characterization of the catalyst material via analysis of an FIB cross-section of the electrode is provided in **Figure S24**. Analysis of the cross-section by SEM and STEM reveals that MoO_x/Ni_{NF} maintained its structure after 110 h operation (**Figures S25-S27)**. This is further corroborated by XPS depth profiling of the post-electrolysis material (**Figures S28**). Here we observe that the Mo 3d and O 1s spectra are almost identical to those recorded on the as-prepared electrode (*cf.* **Figure 4b-c**), indicating that composition of the MoO_x layer is maintained during electrolysis, including the presence of oxygen vacancies and sub-surface Mo(0).

This motivated us to assess the stability of the catalyst at much higher current densities in order to demonstrate the stable and selective electroproduction of NH_3 at industrial-scale reaction rates. We found that MoO_x/Ni_{NF} can maintain a stable reduction potential of about −0.75 V and sustain an average FE_{NH3} of roughly 83% during continuous operation for over 3100 h (i.e. more than 4 months) at −650 mA cm^{-2} (**Figure 7a**). Such long-term stability combined with high FE and yield rate position MoO_x/Ni_{NF} among the best catalysts for NO_3RR in neutral media (**Figure 7b** and **Table S1**).

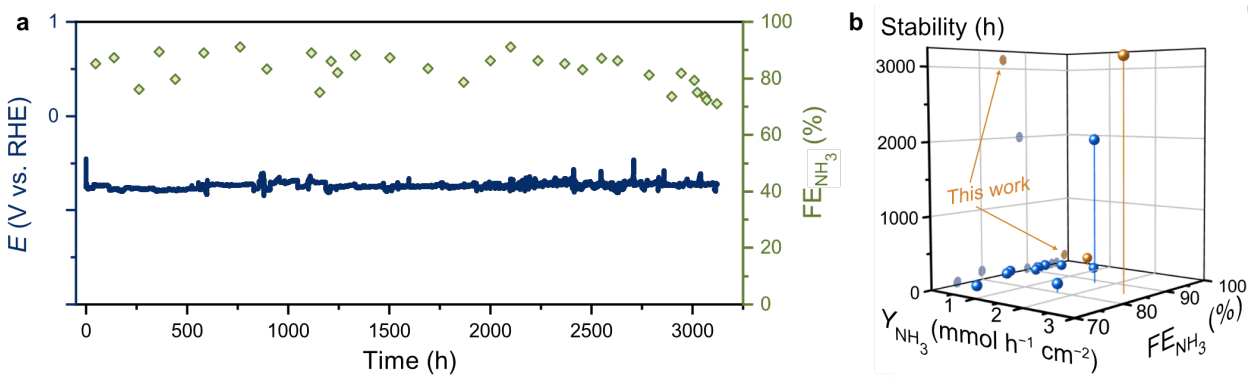

Figure 7. (**a**) Long term stability test of MoO_x/Ni_{NF} in 1 M Na_2SO_4 with 0.1 M NO_3^- at −0.8 V for >3100 h (dark blue line) and the corresponding FE for NH_3 (green rectangles). (**b**) Comparison of the performance of selected previous reported catalysts tested for ≥12 h (blue spheres) with this work (orange spheres). For better comparison the data points are also illustrated on the Stability – FE_{NH3} plane. The corresponding values and references are given in **Table S1**.

Strikingly, after such long operation times, post electrolysis characterization of the materials revealed that the structure and identity of the catalyst was essentially maintained. SEM analysis of the electrode shows that the morphology and structure of the catalyst material is very similar to the original material (**Figure S29**). Post-catalysis analysis of an FIB cross-section of the material revealed that the MoO_x/Ni_{NF} electrode retained its overall morphology even after 3100 hours of use, preserving a Ni core and a MoO_x shell (**Figure S30**). The only noticeable modification in the material structure that could be observed in some areas results from the appearance of some void areas between the MoO_x shell and the core, suggesting the MoO_x shell could be peeling of the catalyst surface after very long operation times (**Figure S31**). We identified a region of the electrode where the thick MoO_x layer appeared to be absent and could have resulted from such a peeling of the shell (**Figure S32**). However, in both this area and in areas close to the partially peeled off MoO_x core, a thin layer of MoO_x is still observed on the catalyst material, suggesting that the materials remained coated by a thin layer of the Mo catalyst. We suspect that this aging of the catalyst material results from the slow Mo dissolution during prolonged electrolysis, potentially exacerbated by localized pH fluctuations. Mo dissolution has been a common issue identified in several Mo-based electrocatalysts.[25] However, the very long operating time investigated here, showing no significant decay of the catalyst performances, and the preservation of the main fraction of the MoO_x shell suggest that the use of the flow cell allows limiting the drift of the electrolyte pH, thus providing a safe and sustainable operating condition for NO_3RR.

Conclusion

In conclusion, we report here the facile preparation of a highly active MoO_x/Ni_{NF} electrocatalyst for NO_3RR through a simple two-step electrodeposition strategy using inexpensive inorganic salts and support. The strategies employed by the nitrate reductase enzyme inspired the design of molybdenum oxides containing oxygen vacancies, which are suspected to facilitate nitrate activation and subsequent reduction pathways, achieving FE values close to unity at −0.5 V, j_{NH3} above −918 mA cm^{-2} at −1.0 V, and long-term stability (more than 4 months). The sustained performance over extended operational periods further underscores the potential of this catalyst system for practical applications in catalytic nitrate reduction.

Acknowledgements

Y-Z.X., D.A. and V. M. thank the European Research Council (ERC) under the European Union's Horizon 2020 research and innovation program (Grant Agreement No. 853064) for support. Y-Z.X. is grateful to the Chinese Scholarship Council for a fellowship. The authors acknowledge ScopeM for their support and especially Peng Zeng and Frank Krumeich for the FIB and TEM contribution.

References

[1] D. Coskun, D. T. Britto, W. Shi, H. J. Kronzucker, *Nat. Plants* **2017**, *3*, 1-10.

[2] a) C. J. Stevens, *Science* **2019**, *363*, 578-580; b) G. E. Oldroyd, O. Leyser, *Science* **2020**, *368*, eaba0196; c) A. Merkoçi, *Nat. Food* **2021**, *2*, 920-921.

[3] a) M. Duca, M. T. Koper, *Energy Environ. Sci.* **2012**, *5*, 9726-9742; b) H. Xu, Y. Ma, J. Chen, W.-x. Zhang, J. Yang, *Chem. Soc. Rev.* **2022**, *51*, 2710-2758; c) M. Ferri, *ACS Energy Lett.* **2024**, *9*, 2394-2400.

[4] M. Duca, M. T. Koper, *Energy Environ. Sci* **2012**, *5*, 9726-9742.

[5] a) J. Liang, Z. Li, L. Zhang, X. He, Y. Luo, D. Zheng, Y. Wang, T. Li, H. Yan, B. Ying, *Chem* **2023**; b) P. H. van Langevelde, I. Katsounaros, M. T. Koper, *Joule* **2021**, *5*, 290-294.

[6] a) J. Li, G. Zhan, J. Yang, F. Quan, C. Mao, Y. Liu, B. Wang, F. Lei, L. Li, A. W. Chan, *J. Am. Chem. Soc.* **2020**, *142*, 7036-7046; b) P. Li, Z. Jin, Z. Fang, G. Yu, *Energy Environ. Sci.* **2021**, *14*, 3522-3531; c) Y. Wang, A. Xu, Z. Wang, L. Huang, J. Li, F. Li, J. Wicks, M. Luo, D.-H. Nam, C.-S. Tan, *J. Am. Chem. Soc.* **2020**, *142*, 5702-5708; d) Y. Wang, W. Zhou, R. Jia, Y. Yu, B. Zhang, *Angew. Chem. Int. Ed.* **2020**, *59*, 5350-5354; e) C. Wang, Z. Liu, T. Hu, J. Li, L. Dong, F. Du, C. Li, C. Guo, *ChemSusChem* **2021**, *14*, 1825-1829; f) R. Daiyan, T. Tran-Phu, P. Kumar, K. Iputera, Z. Tong, J. Leverett, M. H. A. Khan, A. A. Esmailpour, A. Jalili, M. Lim, *Energy Environ. Sci.* **2021**, *14*, 3588-3598; g) J. M. McEnaney, S. J. Blair, A. C. Nielander, J. A. Schwalbe, D. M. Koshy, M. Cargnello, T. F. Jaramillo, *ACS Sustain. Chem. Eng.*

2020, *8*, 2672-2681; h) Y. Guo, R. Zhang, S. Zhang, Y. Zhao, Q. Yang, Z. Huang, B. Dong, C. Zhi, *Energy Environ. Sci.* **2021**, *14*, 3938-3944; i) G.-F. Chen, Y. Yuan, H. Jiang, S.-Y. Ren, L.-X. Ding, L. Ma, T. Wu, J. Lu, H. Wang, *Nat. Energy* **2020**, *5*, 605-613; j) R. Jia, Y. Wang, C. Wang, Y. Ling, Y. Yu, B. Zhang, *ACS Catal.* **2020**, *10*, 3533-3540; k) Z.-Y. Wu, M. Karamad, X. Yong, Q. Huang, D. A. Cullen, P. Zhu, C. Xia, Q. Xiao, M. Shakouri, F.-Y. Chen, *Nat. Commun.* **2021**, *12*, 2870; l) X. F. Cheng, J. H. He, H. Q. Ji, H. Y. Zhang, Q. Cao, W. J. Sun, C. L. Yan, J. M. Lu, *Adv. Mater.* **2022**, *34*, 2205767; m) C. Zhang, Y. Zhang, R. Deng, L. Yuan, Y. Zou, T. Bao, X. Zhang, G. Wei, C. Yu, C. Liu, *Adv. Mater.* **2024**, 2313844; n) J. Ni, J. Yan, F. Li, H. Qi, Q. Xu, C. Su, L. Sun, H. Sun, J. Ding, B. Liu, *Adv. Energy Mater.* **2024**, 2400065; o) R. Zhang, Y. Guo, S. Zhang, D. Chen, Y. Zhao, Z. Huang, L. Ma, P. Li, Q. Yang, G. Liang, *Adv. Energy Mater.* **2022**, *12*, 2103872; p) X. Zhao, Y. Jiang, M. Wang, S. Liu, Z. Wang, T. Qian, C. Yan, *Adv. Energy Mater.* **2023**, *13*, 2301409.

[7] a) C. Correia, S. Besson, C. D. Brondino, P. J. González, G. Fauque, J. Lampreia, I. Moura, J. J. G. Moura, *J. Biol. Inorg. Chem.* **2008**, *13*, 1321-1333; b) C. L. Ford, Y. J. Park, E. M. Matson, Z. Gordon, A. R. Fout, *Science* **2016**, *354*, 741-743; c) C. Sparacino-Watkins, J. F. Stolz, P. Basu, *Chem. Soc. Rev.* **2014**, *43*, 676-706.

[8] a) S. Al-Attar, J. Rendon, M. Sidore, J.-P. Duneau, F. Seduk, F. Biaso, S. Grimaldi, B. Guigliarelli, A. Magalon, *ACS Catal.* **2021**, *11*, 14303-14318; b) J. Rendon, F. Biaso, P. Ceccaldi, R. Toci, F. Seduk, A. Magalon, B. Guigliarelli, S. Grimaldi, *Inorg. Chem.* **2017**, *56*, 4422-4434.

[9] Y. Li, Y. K. Go, H. Ooka, D. He, F. Jin, S. H. Kim, R. Nakamura, *Angew. Chem. Int. Ed.* **2020**, *59*, 9744-9750.

[10] D. F. Abbott, Y. Z. Xu, D. A. Kuznetsov, P. Kumar, C. R. Müller, A. Fedorov, V. Mougel, *Angew. Chem., Int. Ed.* **2023**, *135*, e202313746.

[11] P. Guha, B. Mohanty, R. Thapa, R. Kadam, P. V. Satyam, B. K. Jena, *ACS Appl. Energy Mater.* **2020**, *3*, 5208-5218.

[12] a) W. Hua, H.-H. Sun, F. Xu, J.-G. Wang, *Rare Met.* **2020**, *39*, 335-351; b) I. Roger, M. A. Shipman, M. D. Symes, *Nat. Rev. Chem.* **2017**, *1*, 1-13; c) T. H. Chiang, H. Lyu, T. Hisatomi, Y. Goto, T. Takata, M. Katayama, T. Minegishi, K. Domen, *ACS Catal.* **2018**, *8*, 2782-2788; d) M. Zang, N. Xu, G. Cao, Z. Chen, J. Cui, L. Gan, H. Dai, X. Yang, P. Wang, *ACS Catal.* **2018**, *8*, 5062-5069; e) I. A. De Castro, R. S. Datta, J. Z. Ou, A. Castellanos-Gomez, S. Sriram, T. Daeneke, K. Kalantar-zadeh, *Adv. Mater.* **2017**, *29*, 1701619.

[13] a) S. Lamaison, D. Wakerley, D. Montero, G. Rousse, D. Taverna, D. Giaume, D. Mercier, J. Blanchard, H. N. Tran, M. Fontecave, *ChemSusChem* **2019**, *12*, 511-517; b) S. Lamaison, D. Wakerley, J. Blanchard, D. Montero, G. Rousse, D. Mercier, P. Marcus, D. Taverna, D. Giaume, V. Mougel, *Joule* **2020**, *4*, 395-406; c) T. N. Huan, G. Rousse, S. Zanna, I. T. Lucas, X. Xu, N. Menguy, V. Mougel, M. Fontecave, *Angew. Chem. Int. Ed.* **2017**, *56*, 4792-4796; d) T. N. Huan, D. A. Dalla Corte, S. Lamaison, D. Karapinar, L. Lutz, N. Menguy, M. Foldyna, S.-H. Turren-Cruz, A. Hagfeldt, F. Bella, *Proc. Natl. Acad. Sci. U. S. A.* **2019**, *116*, 9735-9740.

[14] a) W. Tsai, P. Hsu, Y. Hwu, C. Chen, L. Chang, J. Je, H. Lin, A. Groso, G. Margaritondo, *Nature* **2002**, *417*, 139-139; b) A. Dutta, I. n. Zelocualtecatl Montiel, K. Kiran, A. Rieder, V. Grozovski, L. Gut, P. Broekmann, *ACS Catal.* **2021**, *11*, 4988-5003; c) A. Dutta, I. Z. Montiel, R. Erni, K. Kiran, M. Rahaman, J. Drnec, P. Broekmann, *Nano Energy* **2020**, *68*, 104331; d) F. C. Walsh, S. Wang, N. Zhou, *Curr. Opin. Electrochem.* **2020**, *20*, 8-19.

[15] H. Wu, A. Singh-Morgan, K. Qi, Z. Zeng, V. Mougel, D. Voiry, *ACS Catal.* **2023**, *13*, 5375-5396.
[16] a) T. J. Morley, L. Penner, P. Schaffer, T. J. Ruth, F. Bénard, E. Asselin, *Electrochem. commun.* **2012**, *15*, 78-80; b) R. Syed, S. Ghosh, P. Sastry, G. Sharma, R. Hubli, J. Chakravartty, *Surf. Coat. Technol.* **2015**, *261*, 15-20; c) V. Kuznetsov, M. Pavlov, D. Zimakov, S. Chepeleva, V. Kudryavtsev, *Russ. J. Electrochem.* **2004**, *40*, 711-715.
[17] a) S. Wlodek, J. Wulff, *J. Electrochem. Soc.* **1960**, *107*, 565; b) K. S. Farmakis, I. G. Poulios, *Z. Naturforsch. A* **1989**, *44*, 533-537.
[18] A. Haseeb, K. Bade, *Microsyst. Technol.* **2008**, *14*, 379-388.
[19] a) K. K. Upadhyay, T. Nguyen, T. M. Silva, M. J. Carmezim, M. F. Montemor, *Electrochimica Acta* **2017**, *225*, 19-28; b) R. K. K. Reddy, S. Kailasa, B. G. Rani, N. Jayarambabu, H. Yasuhiko, G. V. Ramana, K. V. Rao, *SN Applied Sciences* **2019**, *1*, 1-9.
[20] H. Wan, A. Bagger, J. Rossmeisl, *Angew. Chem. Int. Ed.* **2021**, *133*, 22137-22143.
[21] A. Ianoul, T. Coleman, S. A. Asher, *Anal. Chem.* **2002**, *74*, 1458-1461.
[22] a) N. Sergent, M. Epifani, T. Pagnier, *J. Raman Spectrosc.* **2006**, *37*, 1272-1277; b) K. I. Hadjiivanov, *Catal. Rev.: Sci. Eng.* **2000**, *42*, 71-144; c) J.-Y. Fang, Q.-Z. Zheng, Y.-Y. Lou, K.-M. Zhao, S.-N. Hu, G. Li, O. Akdim, X.-Y. Huang, S.-G. Sun, *Nat. Commun.* **2022**, *13*, 7899.
[23] D. P. Butcher Jr, A. A. Gewirth, *Nano Energy* **2016**, *29*, 457-465.
[24] a) L. Bai, F. Franco, J. Timoshenko, C. Rettenmaier, F. Scholten, H. S. Jeon, A. Yoon, M. Rüscher, A. Herzog, F. T. Haase, *J. Am. Chem. Soc.* **2024**; b) F. Lei, K. Li, M. Yang, J. Yu, M. Xu, Y. Zhang, J. Xie, P. Hao, G. Cui, B. Tang, *Inorg. Chem. Front.* **2022**, *9*, 2734-2740.
[25] a) W. Du, Y. Shi, W. Zhou, Y. Yu, B. Zhang, *Angew. Chem. Int. Ed.* **2021**, *60*, 7051-7055; b) J. A. Bau, S. M. Kozlov, L. M. Azofra, S. Ould-Chikh, A.-H. Emwas, H. Idriss, L. Cavallo, K. Takanabe, *ACS Catal.* **2020**, *10*, 12858-12866; c) J. A. Bau, H. Haspel, S. Ould-Chikh, A. Aguilar-Tapia, J.-L. Hazemann, H. Idriss, K. Takanabe, *J. Mater. Chem. A.* **2019**, *7*, 15031-15035.